

Electronic Supplementary Material (ESI) for Inorganic Chemistry Frontiers.

This journal is © the Partner Organisations 2025

Supporting Information

Tailoring Built-in Electric Field in Cobalt Sulfide/Layered Double Hydroxide Hollow Heterostructured Nanocages Strung by MWCNTs for High-Performance Energy Storage

Shi-Yan Cao^{a, b}, Yan-Cun Dong^b, Yi-Jing He^b, Enke Feng^{a, *}, Xiao-Man Cao^b, Xiaoning Xu^{c, *}, Zhi-Jia Sun^{b, *}

[a] Ningxia Key Laboratory of Green Catalytic Materials and Technology, College of Chemistry and Chemical Engineering, Ningxia Normal University, Guyuan 756000, China

[b] College of Chemistry and Materials Engineering, Bohai University, Jinzhou 121013, China

[c] School of Mathematics and Statistics, Liaoning University, Shenyang 110036, China

1. Experimental details

1.1 Materials

In this study, cobalt nitrate hexahydrate ($\text{Co}(\text{NO}_3)_2 \cdot 6\text{H}_2\text{O}$, $\geq 99\%$), 2-methylimidazole ($\text{C}_4\text{H}_6\text{N}_2$, $\geq 99\%$), nickel nitrate hexahydrate ($\text{Ni}(\text{NO}_3)_2 \cdot 6\text{H}_2\text{O}$, $\geq 99\%$), and thioacetamide (TAA, $\text{C}_2\text{H}_5\text{NS}$, $\geq 99\%$) were sourced from Sigma-Aldrich and used as received without further processing. Potassium hydroxide (KOH, $\geq 90\%$) and anhydrous ethanol ($\text{C}_2\text{H}_6\text{O}$, 99.7%) were supplied by Sinopharm Chemical Reagent Co., Ltd. Polytetrafluoroethylene (PTFE, 60 wt% suspension) was obtained from Shanghai Mackin Biochemical Co., Ltd. and multi-walled carbon nanotubes (MWCNTs) were purchased from Shenzhen Nanotech Port Co., Ltd. Deionized water (DI) was utilized in all experiments.

1.2 Synthesis of Co-MOF and Co-MOF/F-MWCNTs Composites

Functionalized multi-walled carbon nanotubes (F-MWCNTs) were dispersed in 25 mL of methanol via ultrasonication for 30 minutes to form a uniform suspension. Subsequently, 8 mmol of 2-methylimidazole (2-MeIM) was added, and the mixture was ultrasonicated for another 30 minutes to prepare solution A. Meanwhile, 2 mmol of $\text{Co}(\text{NO}_3)_2 \cdot 6\text{H}_2\text{O}$ was dissolved in 25 mL of methanol to form solution B. Solution B was added dropwise to solution A under constant stirring for 30 minutes, followed by static aging at room temperature for 24 hours. The resulting product was collected by centrifugation, washed thoroughly with anhydrous ethanol, and dried in a vacuum oven at 70 °C for 24 hours to obtain Co-MOF/F-MWCNTs as a purple powder. For comparison, Co-MOF/F-MWCNTs with different F-MWCNTs mass ratios were synthesized under identical conditions. F-MWCNTs were added at levels of 0, 0.5, 1, and 2 times the base amount. Samples were designated as Co-MOF (0×F-MWCNTs), MFCH (0.5×F-MWCNTs), MFC (1×F-MWCNTs), and MFCD (2×F-MWCNTs).

1.3 Synthesis of NiCo-LDH/F-MWCNTs Composites

MFC, identified as the template due to its superior electrochemical performance, was ultrasonically dispersed in 50 mL ethanol containing 0.7 mmol $\text{Ni}(\text{NO}_3)_2 \cdot 6\text{H}_2\text{O}$. The mixture was refluxed under stirring for 1 h, then rapidly cooled. The resulting product

was collected by centrifugation, washed thoroughly with anhydrous ethanol, and dried in a vacuum oven at 80 °C for 24 h. The final material, NiCo-LDH/F-MWCNTs, exhibited a color change from purple to green and was designated as LFC.

1.4 Synthesis of Co₃S₄/NiCo-LDH@F-MWCNTs Composites

1.6 mmol of thioacetamide (TAA) and 80 mg of LFC were dispersed in 30 mL of ethanol via sonication to form a homogeneous suspension. The suspension was transferred into a Teflon-line sealed autoclave and heated at 120 °C for 4 h. The resulting product was centrifuged, washed with ethanol, and vacuum-dried at 70 °C for 12 h. The obtained brown composite, Co₃S₄/NiCo-LDH@F-MWCNTs, was designated as SLFC. For comparison, Co₃S₄/F-MWCNTs, designated as SFC, were synthesized under the same conditions using MCF as the template.

1.5 Materials Characterization

The crystal structure and chemical composition of the samples were analyzed using X-ray diffraction (XRD, Bruker D8 Advance) and X-ray photoelectron spectroscopy (XPS, PHI Versa Probe). Morphologies and microstructures of the synthesized materials were observed via scanning electron microscope (SEM, Hitachi S-4800) equipped with an energy-dispersive X-ray spectroscopy (EDS) detector and transmission electron microscope (TEM, JEOL JEM-2100). Specific surface area and pore structure were determined using N₂ adsorption-desorption isotherms (Kubo X1000), with pore size distribution analyzed via the BJH model from the desorption branch. Raman spectra were recorded using a Renishaw Confocal Micro-Raman Spectrometer with 633 nm HeNe laser. Fourier transform infrared (FT-IR) spectra were measured using a Nicolet iS 10 spectrometer.

1.6 Electrochemical characterization

The electrochemical performance was assessed using a CHI660E electrochemical workstation (Shanghai CH Instrument Co., China). Single-electrode measurements were performed in a three-electrode configuration with 6 M KOH as the electrolyte, a Pt plate as the counter electrode, and a Hg/HgO electrode as the reference. Electrochemical impedance spectroscopy (EIS) was carried out at open-circuit

potential with a 10 mV perturbation over a frequency range of 0.01 Hz to 20 KHz. For ASC device measurements, a two-electrode system was employed, with SLFC as the positive electrode, activated carbon (AC) as the negative electrode, a piece of polypropylene membrane as a separator, and 6 M KOH as an electrolyte.

2. Calculations

2.1. Capacitances of Single Electrode

The specific capacitance (C_s) was calculated from the discharge curves using the following equation:

$$C_s = \frac{I \times \Delta t}{m \times \Delta V} \quad (\text{Equation S1})$$

Where, C_s represents the specific capacitance (F g^{-1}), I is the discharge current (A), Δt is the discharge time (s), ΔV is the potential window (V), and m is the mass of the as-synthesized material (g).

2.2. Capacitances of ASC device

The gravimetric capacitance of ASC device was determined from the GCD measurements using Equation S2:

$$C_m = \frac{I \times t}{M \times U} \quad (\text{Equation S2})$$

In this equation, C_m (F g^{-1}) represents the specific capacitance, I is discharge current (A), t is the discharge time (s), U is the potential window (V), M is the total mass of active materials (g).

2.3. Energy density and power density of ASC Device

The energy density (E , Wh kg^{-1}) and power density (P , kW kg^{-1}) of ASC device are calculated using the following equations:

$$E = \frac{1000 \times CM \times U^2}{2 \times 3600}$$

(Equation S3)

$$P = \frac{3600 \times E}{1000 \times t} \quad (\text{Equation S4})$$

S4)

where C_M ($F g^{-1}$) is the specific capacitance and U is the operating voltage (V), t is the discharge time (s).

2.4. Charge balance for ASC Device

Electrochemical measurements of the ASC device were performed in a two-electrode configuration, with SLC as the positive electrode, activated carbon (AC) as the negative electrode, a polypropylene membrane as the separator, and 6 M KOH as the electrolyte. To ensure stable performance, the positive and negative electrodes adhered to the balance principle, determined by the equation S5:

$$\frac{m_+}{m_-} = \frac{C_{s-} \times \Delta V_-}{C_{s+} \times \Delta V_+} \quad (\text{Equation S5)}$$

S5)

Here, m (g), C_s ($F g^{-1}$), ΔV (V) represent the electrode materials mass, specific capacitance and voltage window, respectively. Based on this equation, the optimal mass ratio of SLC and AC was calculated as 1:7.73.

2.5. Randles-Sevcik Equation

The relationship between the peak currents (i_p) and the square roots of the scan rate ($v^{1/2}$) was derived from CV, consistent with the Randles-Sevcik equation:

$$i_p = 2.69 \times 10^5 \times n^{3/2} A D^{1/2} C v^{1/2} \quad (\text{Equation S6})$$

Here, C is the concentration of the reactant, A is the surface area of the electrode, D is the diffusion coefficient, v is the scan rate, n is the number of transfer electrons, and i_p is the peak current.¹

2.6. Dunn Method Analysis

The Dunn method is usually used to separate the contributions of the capacitive elements of the charge storage (including the electrical double-layer effect and fast faradaic contribution from the surface/subsurface) from the diffusion-controlled insertion processes (capacitance arising from slow ion de/intercalation in the bulk structure). The main steps involved in the analysis are as follows:

According to the relationship between the sweep rate (v) and the current response

(*i*) measured in CV curves, the contribution degree of capacitance to the current value can be qualitatively analyzed:

$$i = av^b \quad (\text{Equation S7})$$

$$\log(i) = b\log(v) + \log(a) \quad (\text{Equation S8})$$

where *a* and *b* both are adjustable parameters. The value of *b* is between 0.5 and 1.0, which is calculated by fitting the $\log(i)$ versus $\log(v)$ plot according to Equation (8). Ordinarily, the *b* value approaching 0.5 represents that the charge storage mechanism is dominated by a traditional diffusion-controlled process. But when the *b* value is close to 1.0, the reaction is mainly controlled by the surface capacitance process. For *b* values between 0.5 and 1.0, the charge storage process presents a mixed mechanism.

For a better understanding of the charge storage mechanism, the contribution from the capacitive (k_1v) and diffusion-controlled ($k_2v^{1/2}$) to the current value can be calculated quantitatively according to the following relationship:

$$i(v) = k_1v + k_2v^{1/2} \quad (\text{Equation S9})$$

where *i* (*v*) is the current at a given potential, k_1 and k_2 are fixed for the same electrochemical reaction, and *v* is the scan rate, so the values of both can be evaluated from the slope and intercept of the following formula:

$$i(v)/v^{1/2} = k_1v^{1/2} + k_2 \quad (\text{Equation S10})$$

Therefore, if we plot the $i/v^{1/2}$ at a given potential versus $v^{1/2}$, we should obtain a line with the slope equaling constant k_1 and the y-intercept equaling k_2 , thus giving us a quantitative way of separating the capacitive elements, k_1v , from the bulk reactions, $k_2v^{1/2}$, at each given voltage.²

2.7 DFT calculation

Spin-polarized density functional theory (DFT) calculations were performed using the Device Studio platform, which integrates visualization, modeling, and simulation functionalities. Band structure and density of states (DOS) analysis were carried out using the DS-PAW module. The Perdew-Burke-Ernzerhof (PBE) functional within the generalized gradient approximation (GGA) was adopted, with a plane-wave cutoff

energy set to 500 eV. Structural optimization was achieved using the conjugate gradient method, ensuring convergences criteria of 10^{-5} eV for energy and 0.05 eV/Å for atomic force. Brillouin Zone sampling employed a $2 \times 2 \times 1$ Gamma-centered k-point grid. To accurately describe electron correlation effects, the DFT+U approach, with U parameters of 4.0 eV for Co and 3.5 eV for Ni. For the construction of the the NiCo-LDH/ Co_3S_4 heterojunction, the (001) plane of NiCo-LDH and the (311) plane of Co_3S_4 are selected as the reaction surfaces.

3. Supplementary figures and tables

3.1 Supplementary figures

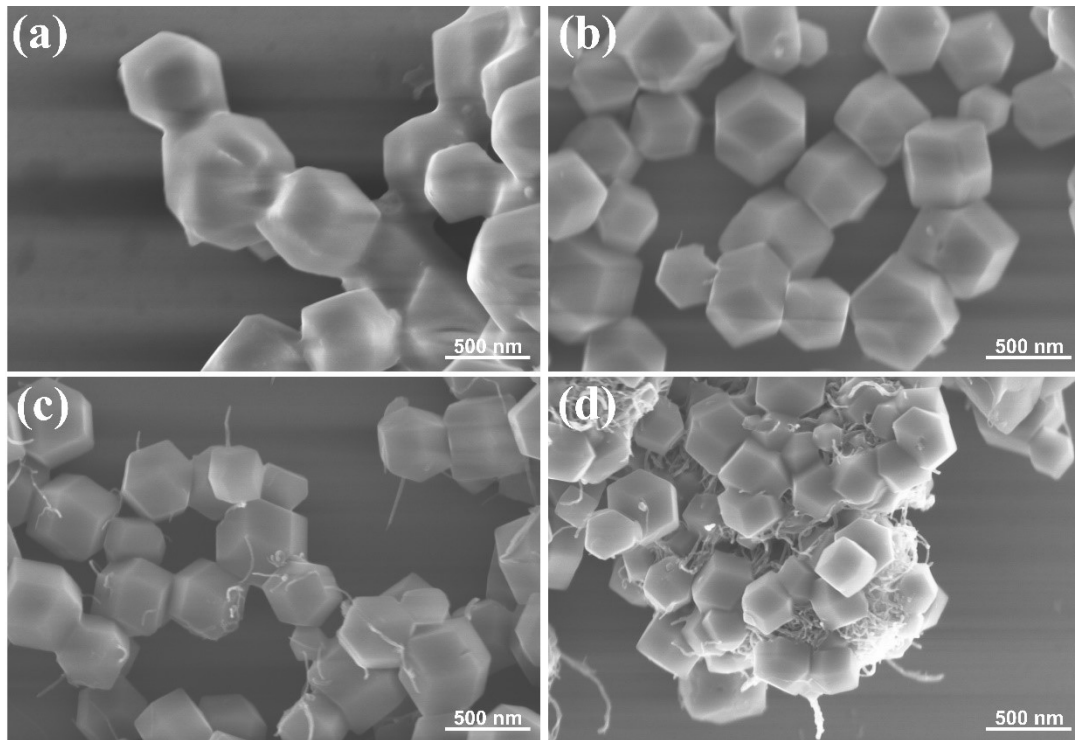


Fig. S1 The SEM patterns of Co-MOF (a), MFCH (b), MFC (c) and MFCD (d).

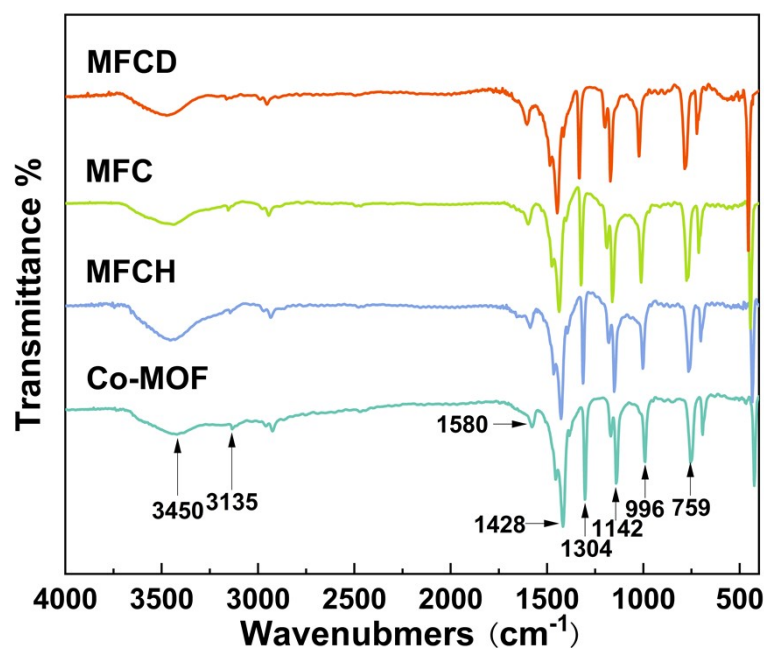


Fig. S2 The FT-IR patterns of Co-MOF, MFCH, MFC and MFCD.

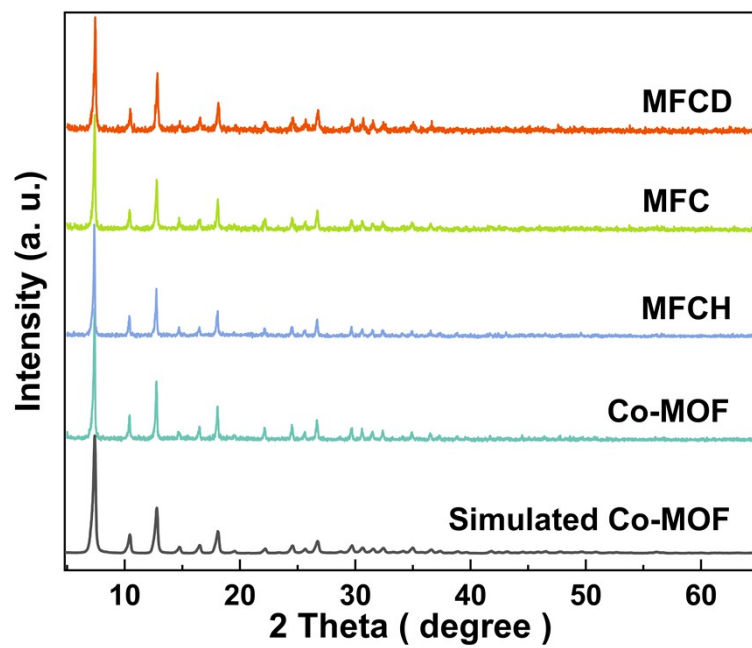


Fig. S3 The XRD patterns of Co-MOF, MFCH, MFC and MFCD.

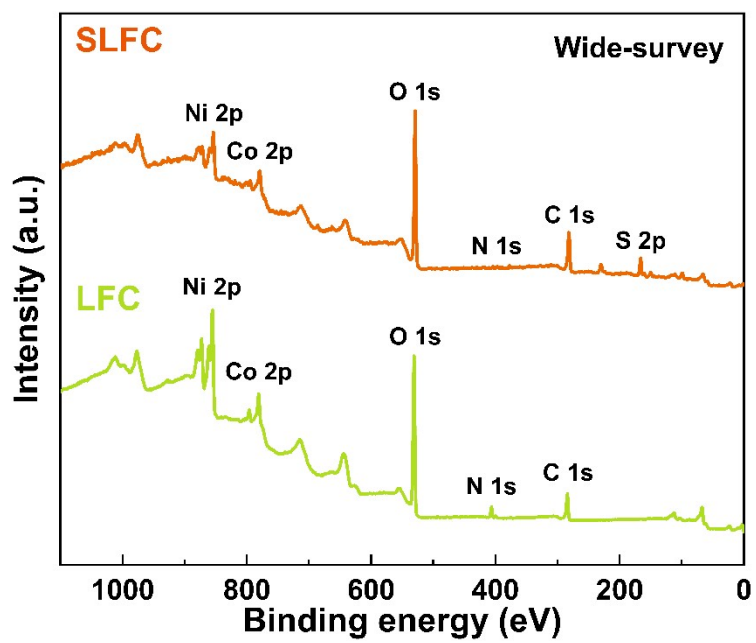


Fig. S4 The full survey XPS spectrum of SLFC and LFC.

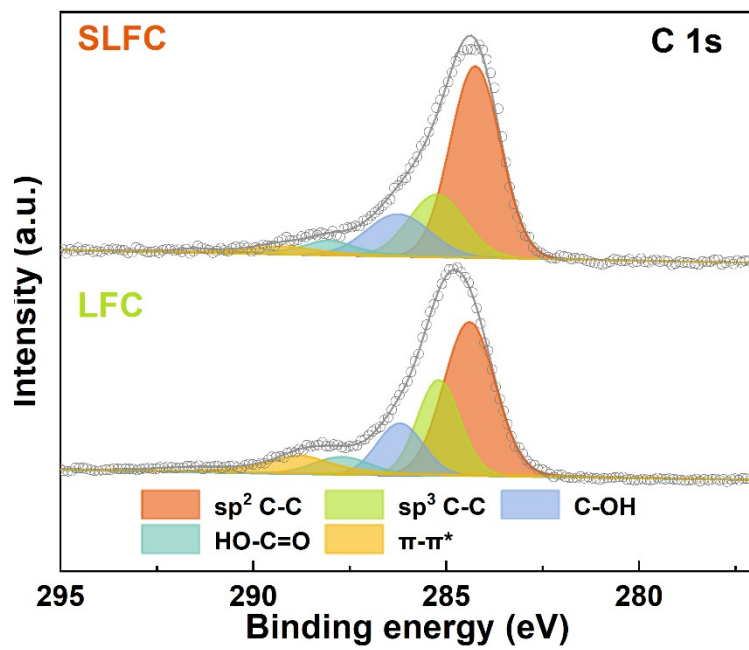


Fig. S5 C 1s XPS spectra of SLFC and LFC.

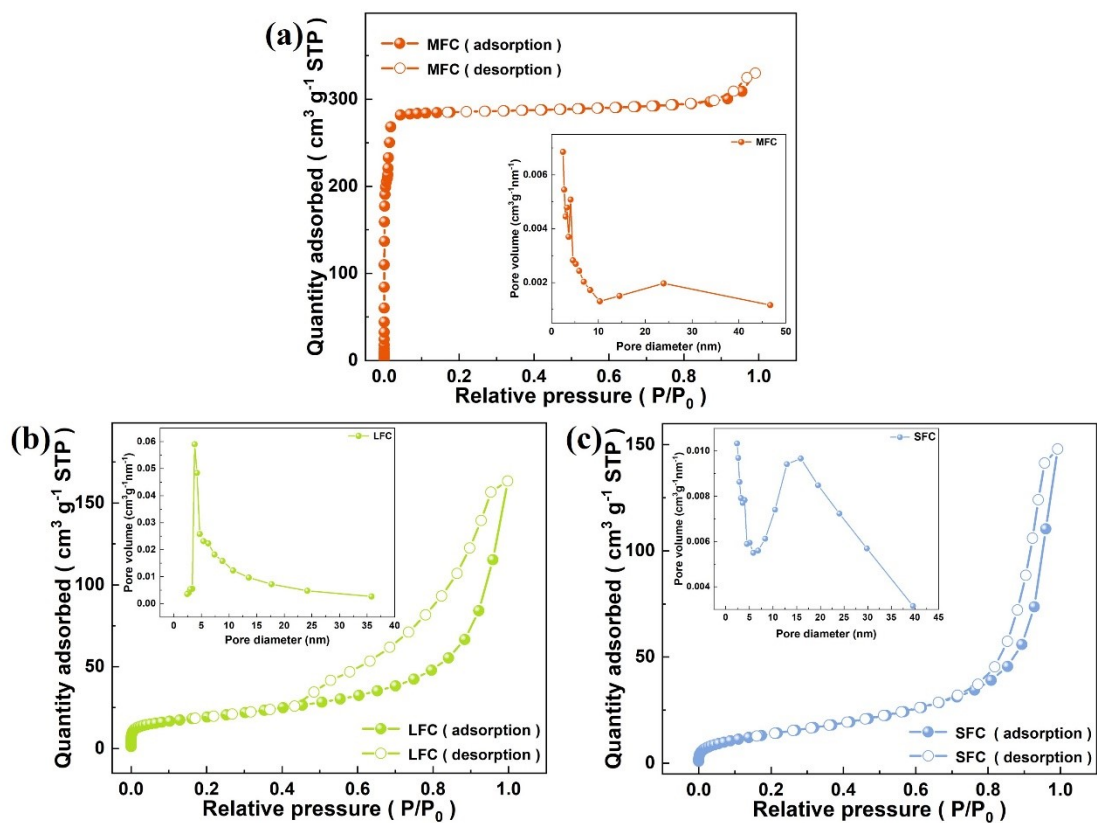


Fig. S6 N_2 adsorption-desorption isotherms of (a) MFC, (b) LFC and (c) SFC.

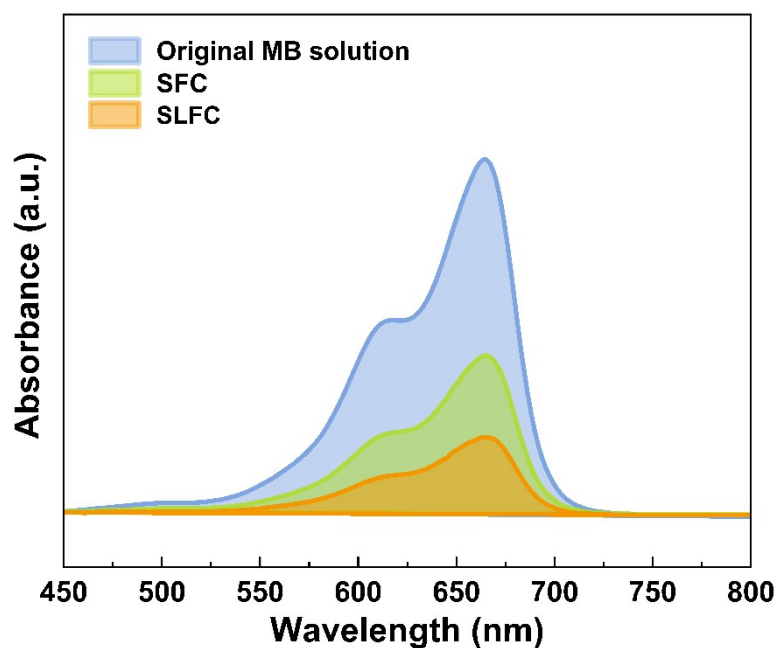


Fig. S7 UV-vis spectra collected for the original MB solution and the MB solutions after reacting with SLFC and SFC.

In order to investigate the surface area of the SLFC and SFC electrodes, methylene blue (MB) adsorption experiments were carried out. Both electrodes were immersed in an 8 mg/L MB water solution in the dark. The UV-Vis absorption spectra of the original MB solution, SLFC and SFC were collected for 24 h under dark conditions. The attenuation of MB characteristic absorption peak intensity (665 nm) of SLFC is greater than that of SFC. The experimental results show that the SLFC electrode has a larger ion-accessible surface area than the SFC electrode.

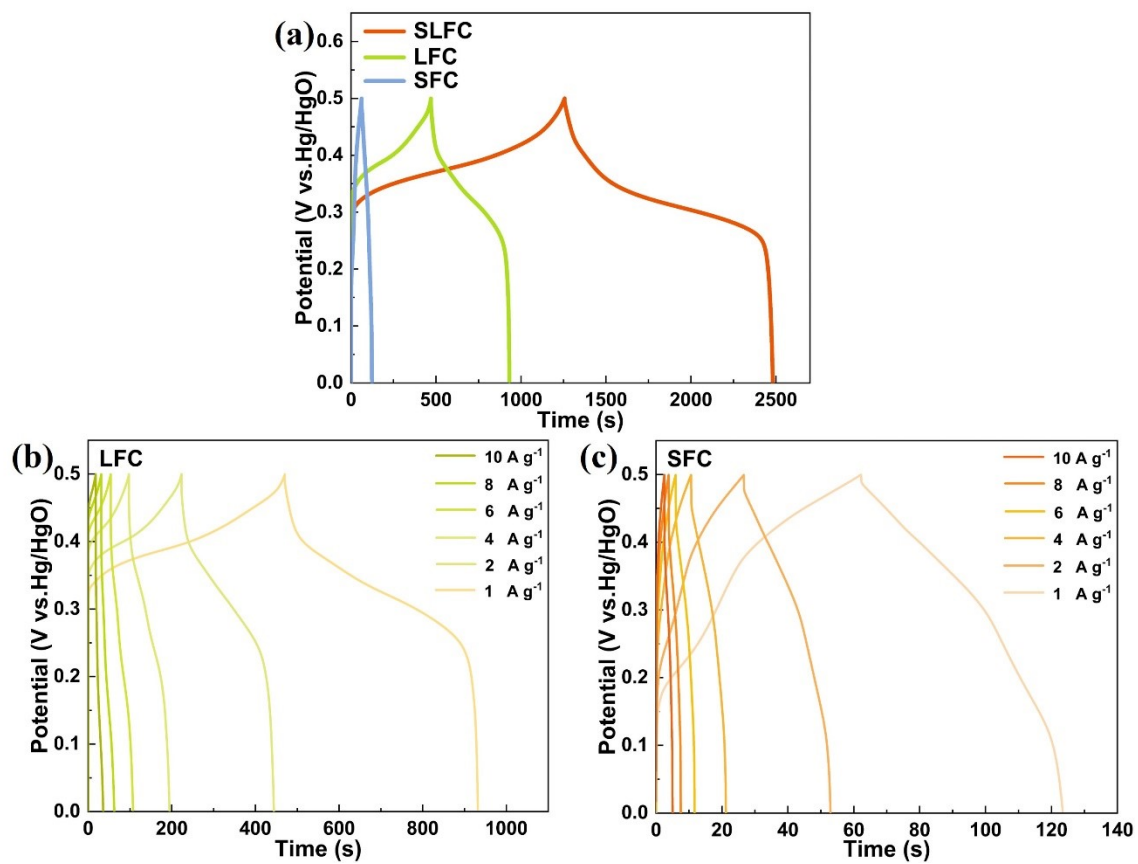


Fig. S8 (a) GCD curves of SFC, LFC and SLFC at 1 A g⁻¹; GCD curves of (b)LFC and (c) SFC at different current densities.

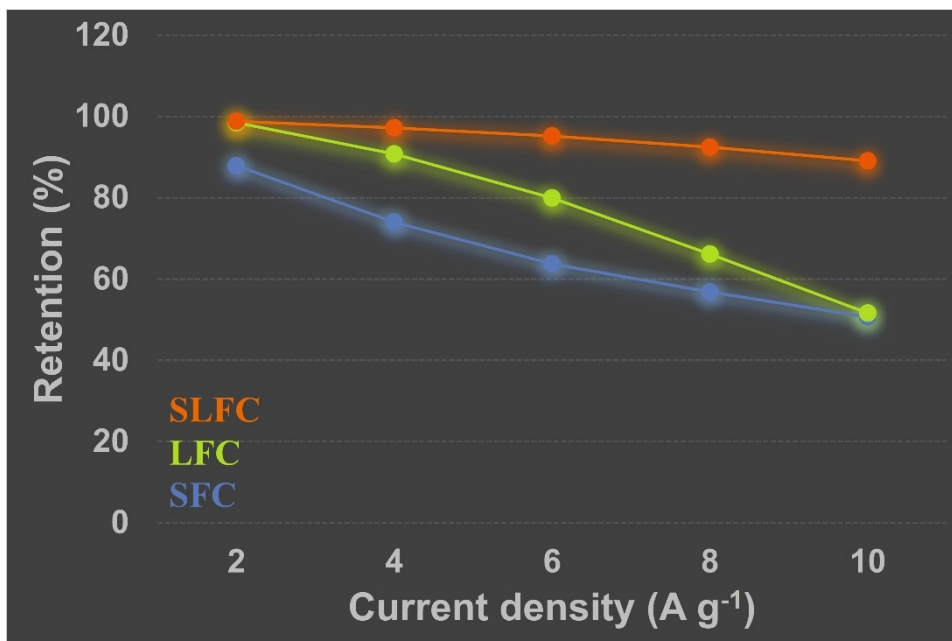


Fig. S9 Rate performance of SLFC, LFC and SFC.

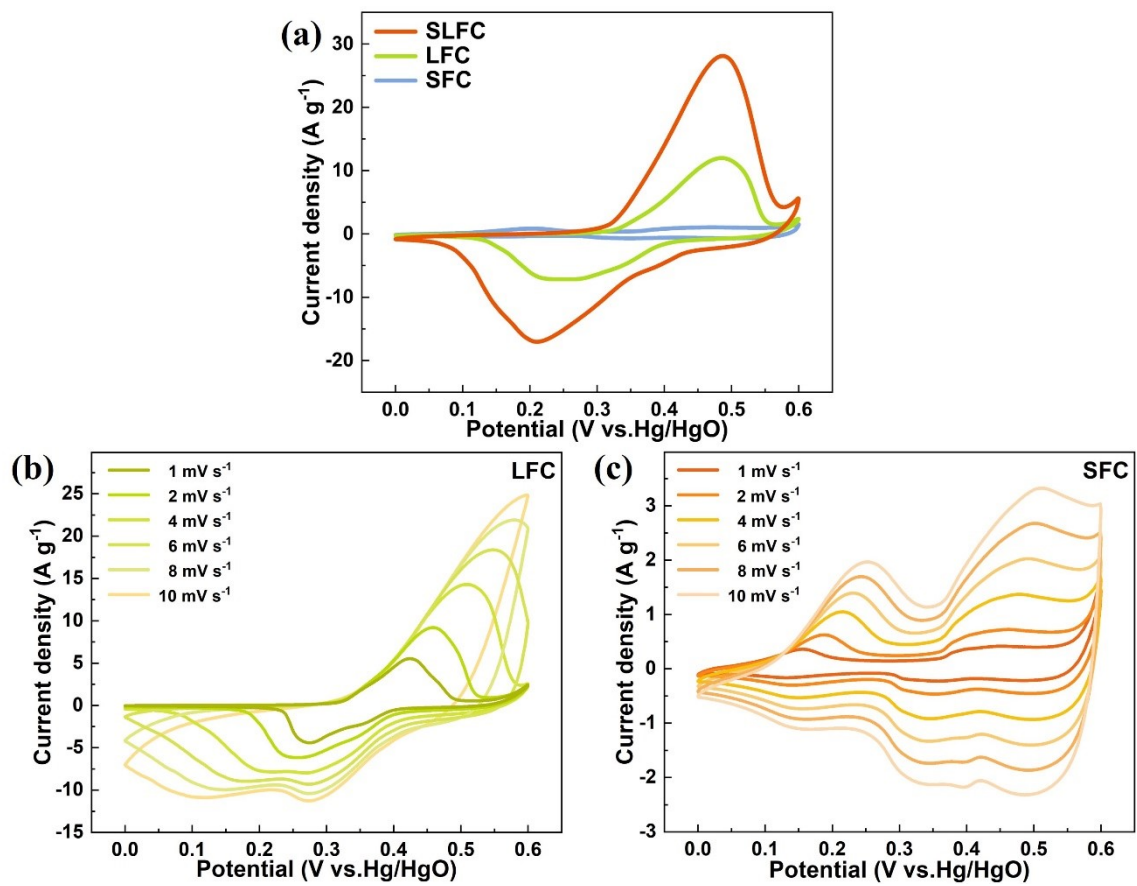


Fig. S10 (a) CV curves of SFC, LFC, and SLFC at 3 mV s⁻¹; CV curves of (b) LFC and (c) SFC at different scan rates.

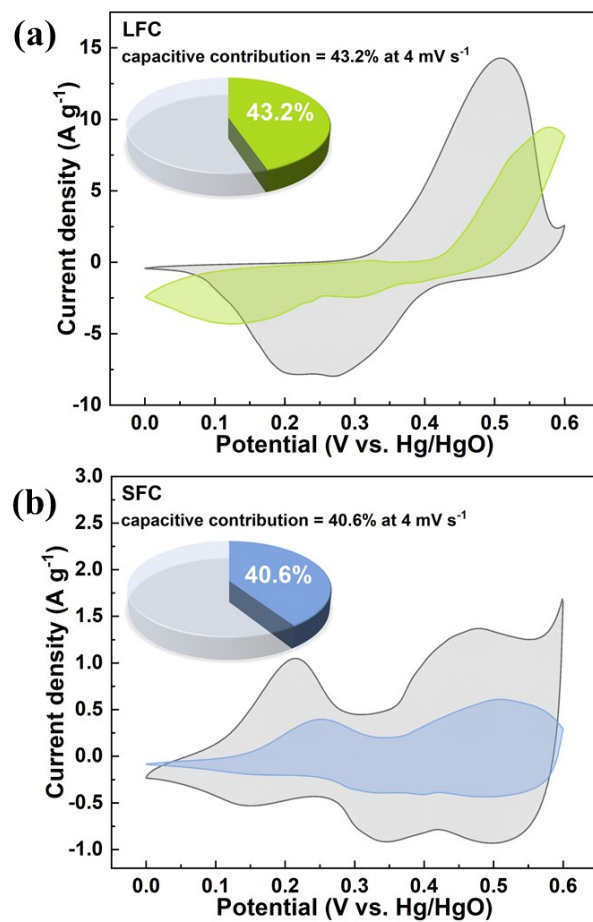


Fig. S11 Capacitive contribution of (a) LFC and (b) SFC electrode at scan rate of 4 mV

s⁻¹.

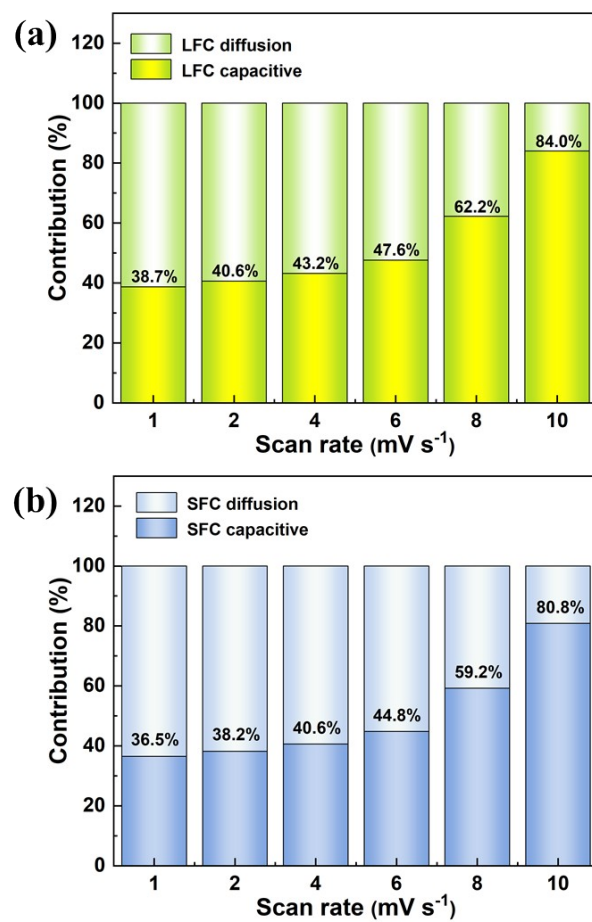


Fig. S12 Capacitive contribution of (a) LFC electrode and (b) SFC electrode.

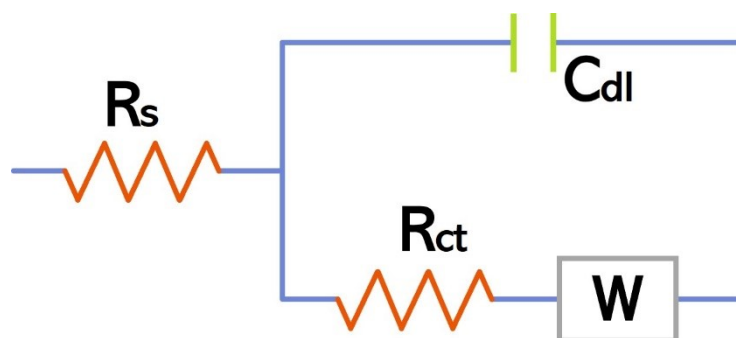


Fig. S13 The fitted equivalent circuit model for the Nyquist plots of SLFC, LFC and SFC.

The equivalent circuit for the Nyquist plots of the samples is displayed in Fig. S13. The intercept of the semicircle with the real axis and the semicircle in the high-frequency region indicates series resistance (R_s , including the internal resistance of the material, electrolyte resistance, and the contact resistance between the electrode material and the current collector) and charge-transfer resistance (R_{ct}). The linear region at low-frequency region represents Warburg impedance (R_w), which signifies ion diffusion/transport from the electrolyte to the electrode surface.

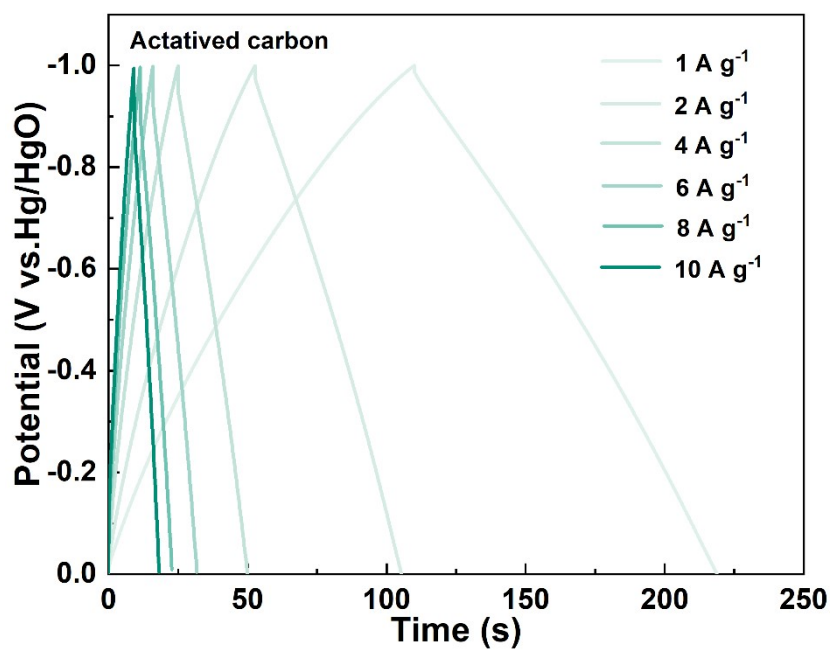


Fig. S14 Galvanostatic charge-discharge profiles of Activated carbon at different current densities.

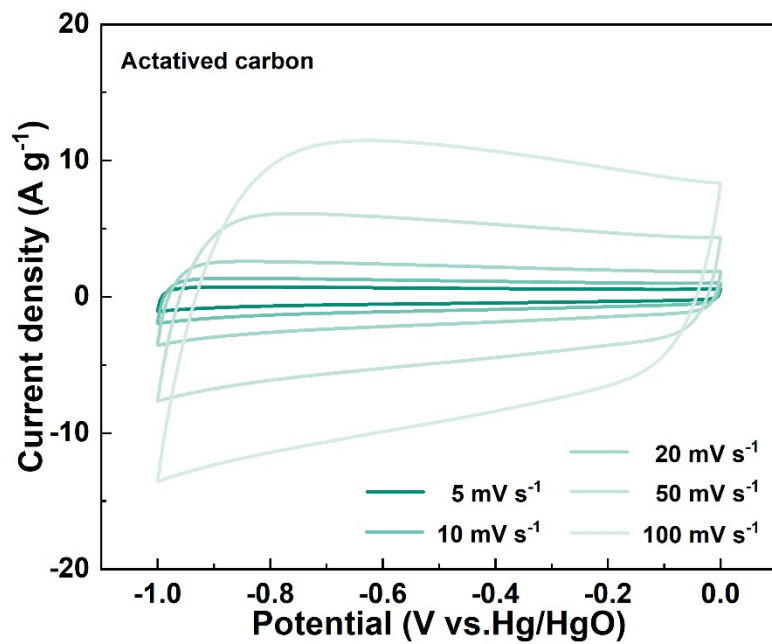


Fig. S15 CV curves of Activated carbon at different scan rates.

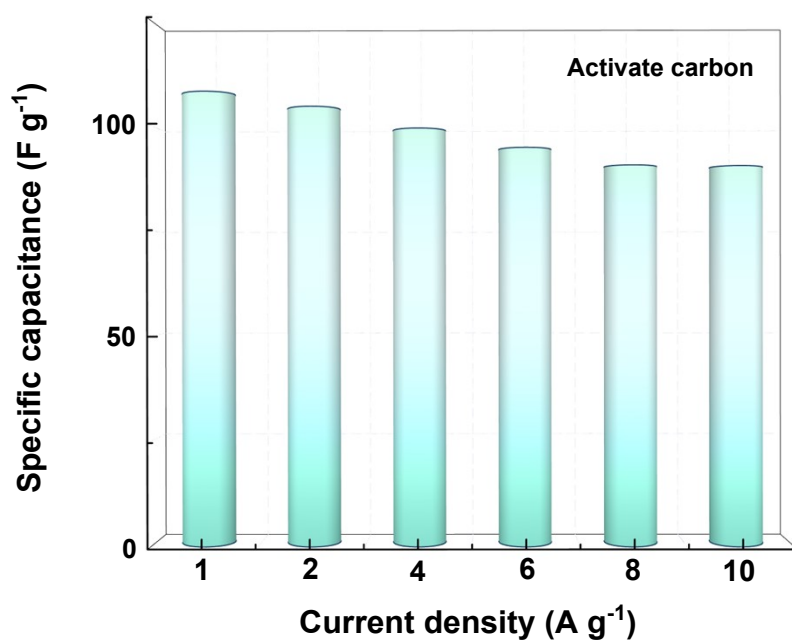


Fig. S16 The specific capacitances of AC at different current density.

3.2 Supplementary tables

Table S1. Specific surface area, pore volume, and average pore size of MFC, LFC, SFC and SLFC.

Sample	Specific Surface Area (m ² g ⁻¹)	Pore Volume (cm ³ g ⁻¹)	Average Pore Size (nm)
MFC	875.8	0.074	5.04
LFC	68.5	0.285	3.98
SFC	52.4	0.238	4.72
SLFC	85.15	0.459	8.81

Table S2. Comparison of rate performances for samples at varied current density.

Sample	Specific capacitance ($F g^{-1}$)						Retention (%)				
	1	2	4	6	8	10	2	4	6	8	10
	A/g	A/g	A/g	A/g	A/g	A/g	A/g	A/g	A/g	A/g	A/g
LFC	1181.9	1163.61	1073.3	943.9	781.8	609.9	98.5	90.8	79.9	66.1	51.6
SFC	156.3	137.3	115.7	99.6	88.7	79.1	87.9	74	63.7	56.8	50.6
SLFC	3092.4	3054.4	3004.6	2942.8	2860.6	2756.3	98.8	97.2	95.2	92.5	89.1
AC	108	104.4	99.2	94.6	90.4	90.2	96.7	95	87.5	83.7	83.5

Table S3. Comparison of specific capacitance with Previous Studies.

Sample	C_{Max}	C_{Min}	Rate capability	Ref.
Leaf-like $CoS_2/N-C$	383 F g ⁻¹ (1 A g ⁻¹)	225.97 F g ⁻¹ (20 A g ⁻¹)	59% (1 A g ⁻¹ ~20 A g ⁻¹)	3
Co_9S_8 /grapheme paper	653 F g ⁻¹ (0.5 A g ⁻¹)	469 F g ⁻¹ (10 A g ⁻¹)	71.8% (0.5 A g ⁻¹ ~10 A g ⁻¹)	4
$NiCo_2S_4$ @graphene hydrogel	1000 F g ⁻¹ (0.75 A g ⁻¹)	801 F g ⁻¹ (6 A g ⁻¹)	80.1% (0.75 A g ⁻¹ ~6 A g ⁻¹)	5
Double-shelled CoS nanoboxes	980 F g ⁻¹ (1 A g ⁻¹)	585 F g ⁻¹ (20 A g ⁻¹)	59.7% (1 A g ⁻¹ ~20 A g ⁻¹)	6
rGO/CoNiS _x /N-C	1028.2 F g ⁻¹ (1 A g ⁻¹)	918.2 F g ⁻¹ (10 A g ⁻¹)	89.3% (1 A g ⁻¹ ~10 A g ⁻¹)	7
$CoS_{1.097}$ nanotube networks	764 F g ⁻¹ (0.5 A g ⁻¹)	237 F g ⁻¹ (10 A g ⁻¹)	31% (0.5 A g ⁻¹ ~10 A g ⁻¹)	8
$Ni_xCo_{1-x}S_{1.097}$ microspheres	867 F g ⁻¹ (0.5 A g ⁻¹)	598.23 F g ⁻¹ (20 A g ⁻¹)	69% (0.5 A g ⁻¹ ~20 A g ⁻¹)	9
$NiCo_2S_4$ polyhedron	1296 F g ⁻¹ (1 A g ⁻¹)	1208 F g ⁻¹ (10 A g ⁻¹)	93.2% (1 A g ⁻¹ ~10 A g ⁻¹)	10
Flower-like Co_9S_8	522 F g ⁻¹ (0.5 A g ⁻¹)	397 F g ⁻¹ (2 A g ⁻¹)	76% (0.5 A g ⁻¹ ~2 A g ⁻¹)	11
Co_3S_4 -HNCs@PPy	1706 F g ⁻¹ (1 A g ⁻¹)	1236 F g ⁻¹ (10 A g ⁻¹)	72.5% (1 A g ⁻¹ ~10 A g ⁻¹)	12
SLFC	3092.43 F g ⁻¹ (1 A g ⁻¹)	2756.3 F g ⁻¹ (10 A g ⁻¹)	89.13% (1 A g ⁻¹ ~ 10 A g ⁻¹)	This work

Table S4. The fitting results of R_s and R_{ct} for LFC, SFC and SLFC electrodes.

Electrodes	LFC	SFC	SLFC
R_s	0.69 Ω	0.86 Ω	0.33 Ω
R_{ct}	1.53 Ω	4.45 Ω	0.24 Ω

Table S5. Comparison of energy density and power density with Previous Studies.

Device	Window (V)	Electrolyte	Energy density (Wh kg ⁻¹)	Power density (W kg ⁻¹)	Ref.
MnCo ₂ O ₄ @Ni(OH) ₂ //AC	1.6	2 M KOH	48	1400	13
MnCo ₂ S ₄ /CC//PCP/rGO	1.6	2 M KOH	43	801	14
Co ₉ S ₈ @Ni(OH) ₂ //AC	1.8	6 M KOH	31.35	252.8	15
CoO/Co ₉ S ₈ //AC	1.5	2 M KOH	46.2	550	16
MnO ₂ @NiCo-LDH/CoS ₂ //AC	1.55	2 M KOH	49.5	391.5	17
Co ₉ S ₈ /NS-C-1.5 h//AC	1.2	6 M KOH	14.85	681.82	18
Vo-NiCo LDH//Fe ₂ O ₃	1.3	3 M KOH	19.5	430	19
ZNC/CWO-10//AC	1.8	2 M KOH	17.41	181.2	20
NCNRs@NCNSs//AC	1.5	6 M KOH	22.81	375	21
Co ₃ O ₄ @Ni-Co LDH//AC	1.6	2 M KOH	46.3	64.2	22
SLFC//AC	1.5	6 M KOH	65.84 33.73	922.5 7637.4	This work

References

- 1 F. Zhu, L. Sun, Y. Liu, W. Shi, Dual-defect site regulation on MOF-derived P-Co₃O₄@NC@Ov-NiMnLDH carbon arrays for high-performance supercapacitors, *J. Mater. Chem. A*, 2022, 10, 21021–21030.
- 2 Q. Zhang, S. Liu, J. Huang, H. Fu, Q. Fan, H. Zong, H. Guo, A. Zhang, In situ selective selenization of ZIF-derived CoSe₂ nanoparticles on NiMn-layered double hydroxide@CuBr₂ heterostructures for high-performance supercapacitors, *J. Colloid Interface Sci.*, 2024, 655, 273–285.
- 3 Q. Chen, J. Miao, L. Quan, D. Cai, H. Zhan, Bimetallic CoNiS_x nanocrystallites embedded in nitrogen-doped carbon anchored on reduced graphene oxide for high-performance supercapacitors, *Nanoscale*, 2018, 10, 4051–4060.
- 4 H. Hu, B. Y. Guan, X. W. Lou (David), Construction of complex CoS hollow structures with enhanced electrochemical properties for hybrid supercapacitors, *Chem.*, 2016, 1, 102–113.
- 5 Y. Gao, L. Mi, W. Wei, S. Cui, Z. Zheng, H. Hou, W. Chen, Double metal ions synergistic effect in hierarchical multiple sulfide microflowers for enhanced supercapacitor performance, *ACS Appl. Mater. Interfaces*, 2015, 7, 4311–4319.
- 6 S. Liu, C. Mao, Y. Niu, F. Yi, J. Hou, S. Lu, J. Jiang, M. Xu, C. Li, Facile synthesis of novel networked ultralong cobalt sulfide nanotubes and its application in supercapacitors, *ACS Appl. Mater. Interfaces*, 2015, 7, 25568–25573.
- 7 Q. Cheng, C. Yang, K. Tao, L. Han, Inlaying ZIF-derived Co₃S₄ hollow nanocages on intertwined polypyrrole tubes conductive networks for high-performance supercapacitors, *Electrochim. Acta*, 2020, 341, 136042.
- 8 Y. Wang, Q. Du, H. Zhao, S. Hou, Y. Shen, H. Li, X. Kong, W. Sun, B. Zhang, S. Li, F. Huo, W. Zhang, Metal-organic framework derived leaf-like CoSNC nanocomposites for supercapacitor electrodes, *Nanoscale*, 2018, 10, 17958–17964.
- 9 Y. Liu, Z. Wang, Y. Zhong, M. Tade, W. Zhou, Z. Shao, Molecular design of mesoporous NiCo₂O₄ and NiCo₂S₄ with sub-micrometer-polyhedron architectures

- for efficient pseudocapacitive energy storage, *Adv. Funct. Mater.*, 2017, 27, 1701229.
- 10 S. N. Tiruneh, B. K. Kang, S. H. Kwag, Y. Lee, M. Kim, D. H. Yoon, Synergistically active NiCo₂S₄ nanoparticles coupled with holey defect graphene hydrogel for high-performance solid-state supercapacitors, *Chem. Eur. J.*, 2018, 24, 3263–3270.
 - 11 L. Yin, L. Wang, X. Liu, Y. Gai, L. Su, B. Qu, L. Gong, Ultra-fast microwave synthesis of 3D flower-like Co₉S₈ hierarchical architectures for high-performance supercapacitor applications, *Eur. J. Inorg. Chem.*, 2015, 14, 2457–2462.
 - 12 D. Xiong, X. Li, Z. Bai, J. Li, Y. Han, D. Li, Vertically aligned Co₉S₈ nanotube arrays onto graphene papers as high-performance flexible electrodes for supercapacitors, *Chem. Eur. J.*, 2018, 24, 2339–2343.
 - 13 Elshahawy, X. Li, H. Zhang, Y. Hu, K. H. Ho, C. Guan, J. Wang, Controllable MnCo₂S₄ nanostructures for high-performance hybrid supercapacitors, *J. Mater. Chem. A*, 2017, 5, 7494–7506.
 - 14 M. Elshahawy, C. Guan, X. Li, H. Zhang, Y. Hu, H. Wu, S. J. Pennycook, J. Wang, Sulfur-doped cobalt phosphide nanotube arrays for highly stable hybrid supercapacitors, *Nano Energy*, 2017, 39, 162–171.
 - 15 F. Zhu, M. Yan, Y. Liu, H. Shen, Y. Lei, W. Shi, Hexagonal prism-like hierarchical Co₉S₈@Ni(OH)₂ core-shell nanotubes on carbon fibers for high-performance asymmetric supercapacitors, *J. Mater. Chem. A*, 2017, 5, 22782–22789.
 - 16 Y. Wang, T. Zhu, Y. Zhang, X. Kong, S. Liang, G. Cao, A. Pan, Rational design of multi-shelled CoO/Co₉S₈ hollow microspheres for high-performance hybrid supercapacitors, *J. Mater. Chem. A*, 2017, 5, 18448–18456.
 - 17 X. Wang, F. Huang, F. Rong, P. He, R. Que, S. P. Jiang, Unique MOF-derived hierarchical MnO₂ nanotubes@NiCo-LDH/CoS₂ nanocage materials as high-performance supercapacitors, *J. Mater. Chem. A*, 2019, 7, 12018–12028.
 - 18 S. Zhang, D. Li, S. Chen, X. Yang, X. Zhao, Q. Zhao, S. Komarneni, D. Yang, Highly stable supercapacitors with MOF-derived Co₉S₈/carbon electrodes for high-rate electrochemical energy storage, *J. Mater. Chem. A*, 2017, 5, 12453–12461.

- 19 Wu, Y. Wu, P. Lee, S. Yougbaré, L. Lin, Ligand incorporating sequence-dependent ZIF67 derivatives as active material of supercapacitor: Competition between ammonia fluoride and 2-methylimidazole, *ACS Appl. Mater. Interfaces*, 2022, 14, 43180–43194.
- 20 R. R. Neiber, J. Kumar, R. A. Soomro, S. Karkus, H. M. Abo-Dief, A. K. Alanazi, A. A. Altahia, Z. M. El-Bahy, NiZnCoO₄/CoWO₄ hybrid composite with improved electrochemical performance for supercapacitor application, *J. Energy Storage*, 2022, 52, 104900.
- 21 K. Zheng, L. Liao, Y. Zhang, H. Tan, J. Liu, C. Li, D. Jia, Hierarchical NiCo-LDH core/shell homostructural electrodes with MOF-derived shell for electrochemical energy storage, *J. Colloid Interface Sci.*, 2022, 619, 75–83.
- 22 Han, Y. Zhao, Y. Shen, Y. Wei, L. Mao, G. Zeng, Co₃O₄ nanowire@ultrathin Ni-Co layered double hydroxide core-shell arrays with vertical transfer channel for high-performance supercapacitor, *J. Electroanal. Chem.*, 2020, 859, 113887.